RESEARCH ARTICLE

MEDICAL PHYSICS

Reproduction of a conventional anthropomorphic female chest phantom by 3D-printing: Comparison of image contrasts and absorbed doses in CT

Patrizia Kunert[1] | Helmut Schlattl[1] | Sebastian Trinkl[1] | Augusto Giussani[1] | Lea Klein[2] | Martin Janich[2] | Detlef Reichert[3] | Gunnar Brix[1]

[1]Department of Medical and Occupational Radiation Protection, Federal Office for Radiation Protection, Oberschleißheim, Germany

[2]Department of Radiation Oncology, Martin Luther University Halle-Wittenberg, Halle (Saale), Germany

[3]Department of Physics, Martin Luther University Halle-Wittenberg, Halle (Saale), Germany

Correspondence
Patrizia Kunert, Externe und interne Dosimetrie, Biokinetik, Abteilung für medizinischen und beruflichen Strahlenschutz, Bundesamt für Strahlenschutz, Ingolstädter Landstr. 1, D-85764 Oberschleißheim, Germany.
Email: pkunert@bfs.de

Abstract

Background: The production of individualized anthropomorphic phantoms via three-dimensional (3D) printing methods offers promising possibilities to assess and optimize radiation exposures for specifically relevant patient groups (i.e., overweighed or pregnant persons) that are not adequately represented by standardized anthropomorphic phantoms. However, the equivalence of printed phantoms must be demonstrated exemplarily with respect to the resulting image contrasts and dose distributions.

Purpose: To reproduce a conventionally produced anthropomorphic phantom of a female chest and breasts and to evaluate their equivalence with respect to image contrasts and absorbed doses at the example of a computed tomography (CT) examination of the chest.

Methods: In a first step, the effect of different print settings on the CT values of printed samples was systematically investigated. Subsequently, a transversal slice and breast add-ons of a conventionally produced female body phantom were reproduced using a multi-material extrusion-based printer, considering six different types of tissues (muscle, lung, adipose, and glandular breast tissue, as well as bone and cartilage). CT images of the printed and conventionally produced phantom parts were evaluated with respect to their geometric correspondence, image contrasts, and absorbed doses measured using thermoluminescent dosimeters.

Results: CT values of printed objects are highly sensitive to the selected print settings. The soft tissues of the conventionally produced phantom could be reproduced with a good agreement. Minor differences in CT values were observed for bone and lung tissue, whereas absorbed doses to the relevant tissues were identical within the measurement uncertainties.

Conclusion: 3D-printed phantoms are with exception of minor contrast differences equivalent to their conventionally manufactured counterparts. When comparing the two production techniques, it is important to note that conventionally manufactured phantoms should not be considered as absolute benchmarks, as they also only approximate the human body in terms of its absorption, and attenuation of x-rays as well as its geometry.

KEYWORDS
3D-printing, anthropomorphic phantom, quality assurance, X-ray imaging

1 | INTRODUCTION

Commercially fabricated anthropomorphic body phantoms are widely used in x-ray imaging to assess the quality and contrast characteristics of acquired images and to determine absorbed doses in different organs of the body. However, the phantoms are available only in standardized body sizes; thus, they are not appropriate to realistically simulate examinations of underweight and overweight individuals, pregnant women at different stages of gestation, or children of different ages and statures. Moreover, the acquisition costs of the phantoms are high. Therefore, a rapid and cost-effective method to produce individualized anthropomorphic body phantoms based on CT or MRI datasets of actual patients or appropriate virtual 3D-models is highly desirable to optimize diagnostic image quality and measure absorbed doses. Owing to advances in three-dimensional (3D) printing technologies in recent years, this goal can now be achieved. However, this approach still needs to be validated in detail using concrete examples.

The material extrusion-based (MEX) additive manufacturing method, often also referred to as fused-deposition-modeling, is a common 3D-printing technology suitable for the production of body phantoms, where a thermoplastic filament is extruded through a heated print head into single layers of a 3D-object on a build plate. The technology permits the use of comparatively low-budget printers and allows the processing of a broad range of different materials. With professional equipment, the simultaneous processing of multiple materials to print different types of tissues is possible.[1,2] This printing method is common for the production of phantoms for x-ray imaging and therapy.[3-6] By reducing the density of the interior area (infill density), printed objects can be used to mimic the physical properties of different tissues.[7-9] Despite the advantages mentioned, 3D-printing of body phantoms is still at the experimental level. This in particular applies to the selection of print materials and settings.

In a previous study, we investigated a broad range of different commercially available MEX filaments in terms of their attenuation and absorption characteristics for x-ray spectra typically used for diagnostic imaging.[10] As a result, polylactide (PLA) was identified as the best equivalent material to skeletal muscle, acrylonitrile butadiene styrene (ABS) and nylon as best surrogates for adipose tissue, and PLA samples printed with a line pattern with an infill density of 40 % were equivalent to lung tissue. Other materials, for example, polymethylmethacrylate (PMMA) or polyethylene terephthalate glycol (PETG) were characterized as similar to soft tissues, but show slightly different attenuation behaviors than PLA. No suitable material was found for cortical bone in this study; however, stone-filled materials demonstrated similar properties as bones with lower density (spongiosa).

Although various studies addressing patient-specific printed phantoms have been published,[5,11-14] only few studies have performed detailed comparisons to conventionally produced anthropomorphic phantoms.[1,2,15,16] In the latter studies, computed tomography (CT) values (given in Hounsfield units [HU]) of reference phantoms could be reproduced with sufficient accuracy. However, the dosimetric characteristics of printed phantoms were verified for radiation therapy only,[2] but not for x-rays in the energy range typically used in diagnostic imaging.

After the characterization of the attenuation and absorption properties of commercially available print materials in our previous study, the present study aims to reproduce a conventionally fabricated body phantom of the chest and the breasts of a woman through MEX printing and to compare image contrasts as well as absorbed doses at the example of a typical chest CT examination. Moreover, the effect of different print settings (speed, pattern, and infill density) was also systematically investigated.

2 | MATERIALS AND METHODS

All prints were performed using an industrial MEX printer (3ntr A2 V4; 3ntr, Oleggio, Italy) permitting to print three different materials in one step with three 0.6 mm nozzles. The individual print settings were adjusted in the slicing software (Cura 4.3.0; Ultimaker B.V., Geldermanser, Utrecht, Netherlands). CT data were acquired at a multi-slice system with 16 detector rows (GE Bright Speed; General Electrics, Boston, Massachusetts, USA) and images were iteratively reconstructed using a standard kernel.

2.1 | Evaluation of print settings

Cubic samples with a size of $30 \times 30 \times 30$ mm^3 were printed using PLA filaments (PLA; Filamentworld, Neu-Ulm, Germany) in a line infill pattern with the following settings:

1. Print bed temperature: 60°C
2. Material printing temperature: 200°C
3. Infill density: ten different values between 15% and 100%. These samples were printed without compact outer sample boundaries.
4. Printing speed: four different values between 20 and 80 mm/s.
5. Heights of single print layers: 0.1 and 0.2 mm. Larger heights decrease the printing time and the spatial resolution perpendicular to the build plate.

TABLE 1 Parameter settings used to print six sets of PLA samples to systematically evaluate their effect on CT values.

Set Nr.	Infill densities (%)	Printing speeds (mm/s)	Layer height (mm)	Processing mode	Distance from the print bed center; x-, y-direction (cm)
Set 1	15, 25, 35, 45, 55, 65, 75, 85, 95, 100	80	0.2	Simultaneous	(−6.3, 6.3), (0, 6.3), (6.3, 6.3), (−6.3, 0), (0, 0), (6.3, 0), (−6.3, −6.3), (0, −6.3), (6.3, −6.3), (−6.3, −12.72), according to the different infill densities
Set 2	15, 25, 35, 45, 55, 65, 75, 85, 95, 100	40	0.2	Simultaneous	As above
Set 3	15, 35, 55, 75, 95, 100	40	0.2	Serial	(0,0)
Set 4	100	20, 40, 60, 80	0.2	Serial	(0,0)
Set 5	100	20, 40, 60, 80	0.1	Serial	(0,0)
Set 6	100	60	0.2	Simultaneous	(−12.7, 12.7), (−6.3, 6.3), (0, 0), (6.3, −6.3), (12.7, −12.7)
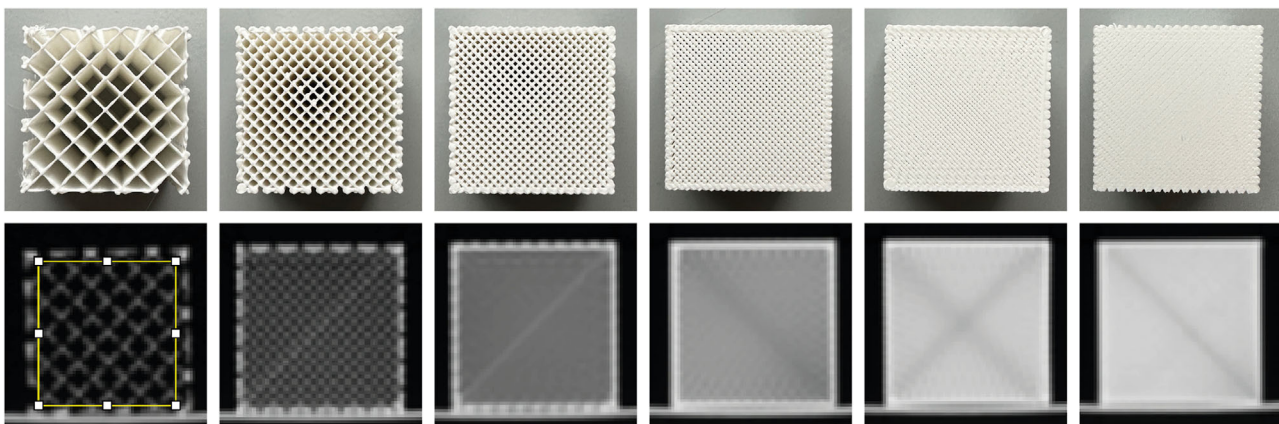
FIGURE 1 Upper row: Cubic test samples of Set 3 (cf. Table 1) printed with infill densities of 15%, 35%, 55%, 75%, 95%, and 100%. Lower row: CT images of the samples (window: width = 1300 HU, center = −350 HU). The slight artifacts are owing to the printing scheme. The rectangular region in the first CT image shows the ROI used to estimate CT values and standard deviations.

6. Processing modes: Simultaneous printing mode (all samples are printed in one run at different positions on the build plate) or serial printing mode (samples are printed in separate runs at the same position on the build plate).
7. Position on the build plate: five different distances from the center of the build plate arranged on a diagonal line (top left to bottom right).

To systematically investigate the effect of the different print settings at the CT value of printed objects, these samples are organized in six sets, as summarized in Table 1. By way of example, Figure 1 shows the samples for Set 3 together with the corresponding CT images.

All 39 samples were separately imaged at the same position of the CT system (axial scan mode; tube voltage, 120 kV; tube current, 200 mA; rotation time, 0.8 s; slice thickness, 1.25 mm; field of view [FOV], 500 mm; reconstructed voxel size, $0.7 \times 0.7 \times 1.25$ mm^3). The samples were aligned with the air ducts of the infill

pattern parallel to the scan direction. CT values were evaluated using the ImageJ software[17] for identical quadratic regions of interest (ROI) with a size of 25×25 mm^2 without inclusion of the boundary regions (cf. Figure 1). The calculated mean values and standard deviations are strongly affected by the infill density and thus characterize the inhomogeneity of the print samples.

2.2 │ Reproduction of conventional anthropomorphic body phantom parts through 3D-printing

A conventionally fabricated anthropomorphic body phantom of a slim woman (height, 173 cm; weight, 55 kg) consisting of axial slices with a thickness of 2.5 cm each and separate breast add-ons (Atom Model 702; CIRS Inc., Norfolk, USA) was used as the template for the production of corresponding 3D-printed phantom parts
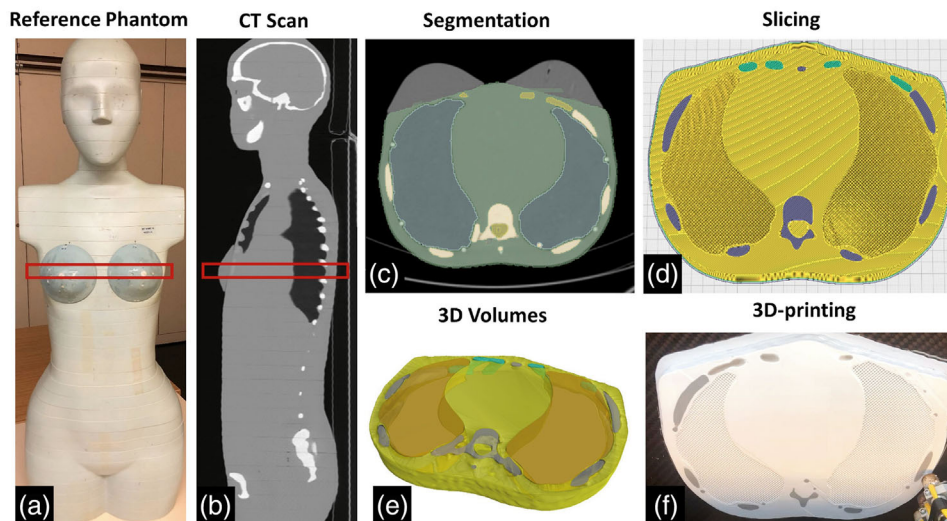
FIGURE 2 Major steps in the production of the 3D-printed axial phantom slice based on a CIRS atom female phantom. The relevant steps (a–f) are described in the text.

(Figure 2a). Specifically, an axial slice in the middle of the chest containing all relevant tissues (with exception of subcutaneous fat) as well as the breast add-ons were reproduced through 3D-printing.

To this end, the following steps were performed: First, a whole-body CT scan of the conventional phantom (helical scan mode; tube voltage, 120 kV; tube current, 50 mA; rotation time, 1.0 s; detector width, 10 mm; pitch; 1.375; FOV, 500 mm; reconstructed voxel size, 0.98 × 0.98 × 0.63 mm^3) was performed (Figure 2b). Second, the different tissues in the considered slice, respectively the breast add-ons were segmented according to their different CT values from the acquired CT dataset using the threshold function of the program 3D slicer[18] (Figure 2c). Third, the segmented 3D volumes (Figure 2e) were improved (e.g., smoothing of surfaces), which was performed using a computer aided design (CAD) software (Rhinoceros 5; Robert McNeel & Associates, Seattle, Washington, USA). Additionally, a simplified glandular structure in form of a parabolic volume was constructed for one breast add-on in this step. Thereafter, printing materials and the corresponding print settings were assigned to the segmented tissue volumes in the slicing software (Figure 2d), and the actual printing step was performed (Figure 2f).

For the axial phantom slice, PLA was used to reproduce the muscle and lung tissue, in the latter case with a reduced infill density and the line infill pattern. A granite-PLA composite filament was chosen to represent a mean bone composition (consisting of a mix of cortical bone, spongiosa, and bone marrow), and PETG for cartilage tissue, because of its comparatively larger attenuation than PLA.[10] ABS was used to reproduce the adipose tissue of the breast add-ons, whereas PMMA served as the material for the glandular structure in one breast

add-on. The print settings for all mentioned materials are summarized in Table 2 based on the results of the pre-examinations described above. Therefore, the used infill-density for the representation of the lung tissue (30%) deviated to some extent from our previous investigations on the tissue equivalence (40%).[10]

Pins with a diameter of 7 mm were separately printed for all materials considered. In each of the pins, a bore hole with a diameter of 2 mm and a depth of 7 mm was drilled to accommodate rod shaped thermoluminescence dosimeter (TLD). With these dimensions air pockets around inserted TLDs were minimized, but nevertheless allow comfortable insertion and removal of the TLDs. The pins with the TLDs were inserted into holes drilled in the printed phantom parts at the same location as in the conventional phantom parts (cf. Figure 5). This way, for dose measurements, four, ten, and seven TLDs can be located inside the muscle tissue area, lungs, and bones of the printed slice, respectively, whereas four TLDs can be located in each printed breast add-on.

2.3 | Evaluation of CT values and absorbed doses

To investigate the image contrasts and absorbed doses in the conventionally produced and the printed slice as well as the breast add-ons, five phantom slices with a thickness of 2.5 cm and the breast add-ons were fixed together by an adhesive tape to minimize air gaps. Axial CT images (tube voltage, 120 kV; tube current, 100 mA; rotation time, 0.8 s; slice thickness, 0.63 mm; FOV, 500 mm; reconstructed voxel size, 0.7 × 0.7 × 0.63 mm^3) were acquired: once with the conventionally produced CIRS phantom parts and once with the

TABLE 2 MEX filaments and corresponding print settings used for 3D-printing of the considered body regions.

Material	Substitute for	Filament name	Printing temperature (°C)	Heat bed temperature (°C)	Print speed (mm/s)	Infill density (%)
Chest phantom slice						
PLA	Muscle and lung tissue	PLA snow white[1]	200	60	60	95 for muscle tissue and 30 for lung tissue
Granite- PLA	Bones	Stonefil granite[2]	220	60	60	100
PETG	Cartilage	PETG natural[3]	230	110	80	100
Breast add-ons						
ABS	Adipose tissue	ABS grey[1]	240	110	80	100
PMMA	Glandular tissue	PMMA transparent[4]	230	110	80	100

Manufacturer: 1) Filamentworld, 2) Formfutura, 3) Renkforce, and 4) Material4print.

FIGURE 3 Experimental setup for the chest CT scan of the 3D-printed phantom parts (printed slice in the middle). A similar scan containing the conventionally manufactured phantom parts was additionally performed.

printed parts (Figure 3). To ensure that scattered x-rays are considered in the examination, the phantom parts to be investigated were surrounded by two CIRS slices on either side. For both phantom settings, CT values were evaluated in selected ROIs and along line profiles.

Absorbed doses in the two phantoms were measured with TLDs (LiF:Mg, Ti, TLD-100; Bicron-Harshaw, Cleveland, Ohio, USA). In total, 29 TLD rods were inserted in each phantom and 10 TLD chips were attached ventral and dorsal on the phantom surface to measure the skin dose. To obtain a sufficient signal on the TLDs, the scans were repeated four times each. The dose absorbed in the different tissues was determined by the mean of the relevant TLD readings.

Annealing and the read-out of the TLDs was performed using a suitable oven (TLDO 1321; PTW-Freiburg, Freiburg, Germany) and reader (Harshaw TLD 5550; Thermo Fischer Scientific, Waltham,

Massachusetts, USA). Each TLD was calibrated by irradiation with an industrial x-ray tube (Comet 320, MXR-320/26AX; Comet, Flamatt, Switzerland) at a tube voltage of 120 kV and a beam with first half-value layer of 7.9 mm aluminum-equivalent, corresponding to the filtration of the CT scanner. TLDs were calibrated (dose in water) using a calibrated stem chamber (M23331; PTW-Freiburg, Freiburg, Germany). Based on repetition measurements, the uncertainty of TLD measurements was estimated with 4%.[19]

3 | RESULTS

3.1 | Evaluation of print settings

Exemplarily for Set 3, CT images of the samples are presented in Figure 1 demonstrating the concept of reducing CT values by lowering the infill densities. The visible diagonal lines are owing to the printing scheme, which starts with the innermost diagonal line that has therefore less adhesion to the neighbor line printed as the last in the respective layer. The actual CT values evaluated for identical ROIs placed over the different sets of printed cubes are plotted versus the infill density, printing speed, and position on the build plate in Figures 4a–c.

Figure 4a shows that CT values increase linearly with increasing infill densities, whereas the standard deviations are higher for lower infill densities, owing to the less homogeneous material distribution. However, the printing speed (Set 2) and mode (Set 3) affect the linear relationship between CT and infill densities slightly by increasing the CT values for higher infill densities. Figure 4b demonstrates that CT values decrease linearly with increasing print speed. This effect is markedly higher for larger (Set 4) than for smaller (Set 5) layer heights. The standard deviation for CT values was markedly higher for the faster print speeds, indicating a lower printing accuracy
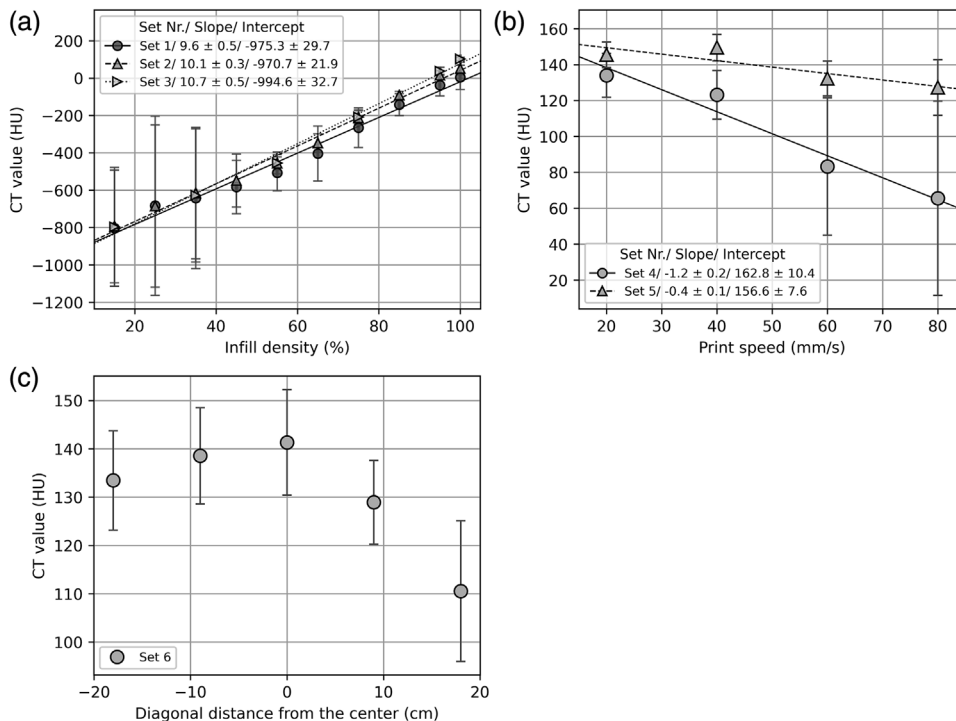
FIGURE 4 CT values measured in printed sample cubes in dependence on (a) the infill density for different printing speeds and modes, (b) the printing speed for two different layer heights, and (c) the diagonal distance on the build plate from its center. Lines indicate the results of linear regression analyses for which the parameters and their corresponding standard errors are given in the legends; error bars indicate the standard deviation of CT values within the selected ROIs.

with less homogeneous material distribution in the samples.

Figure 4c shows that CT values vary substantially for samples printed at different positions of the build plate indicating issues with the build plate leveling of the used printer.

3.2 | Comparison of 3D-printed and conventionally produced phantom parts

The phantom slice was 3D-printed with 864 g of PLA, 80 g of granite-PLA composite, and 11 g of PETG in 43 h; the breast add-ons were printed with 205 g of ABS, respectively 160 g of ABS and 38 g of PMMA each in approximately 15 h. The print settings used are summarized in Table 2. The total costs of the materials were 39€; however, the corresponding machine price and working hours are additional costs not considered in this calculation. The simultaneous processing of the different filament materials was conducted without problems and the different materials exhibited a good adhesion in the finished prints.

The printed phantom slice of the chest and the breast add-ons, as well as the corresponding parts of the conventional phantom are shown in Figure 5.

The circumference of the printed phantom slice was 5 mm longer than that of the conventional phantom

FIGURE 5 Conventionally produced (left) and printed (right) phantom slices and breast add-ons (the printed add-on on the right side contains the glandular structure). For the printed phantom slice, there is no individual color coding for the lung tissue, and the infill pattern is not directly visible because the phantom slice is sealed with a thin layer of fully printed material. The positions for insertion of TLDs are marked with colored circles (red = bones, blue = lungs, green = muscle, yellow = breasts).

slice, but their height was equal. This is because of the less smooth body surface of the printed phantom slice reasoned in the segmentation process. In contrast, the circumferences at the chest wall and the height of the printed breast add-ons were 10 and 3 mm smaller compared to those of the conventionally produced breast
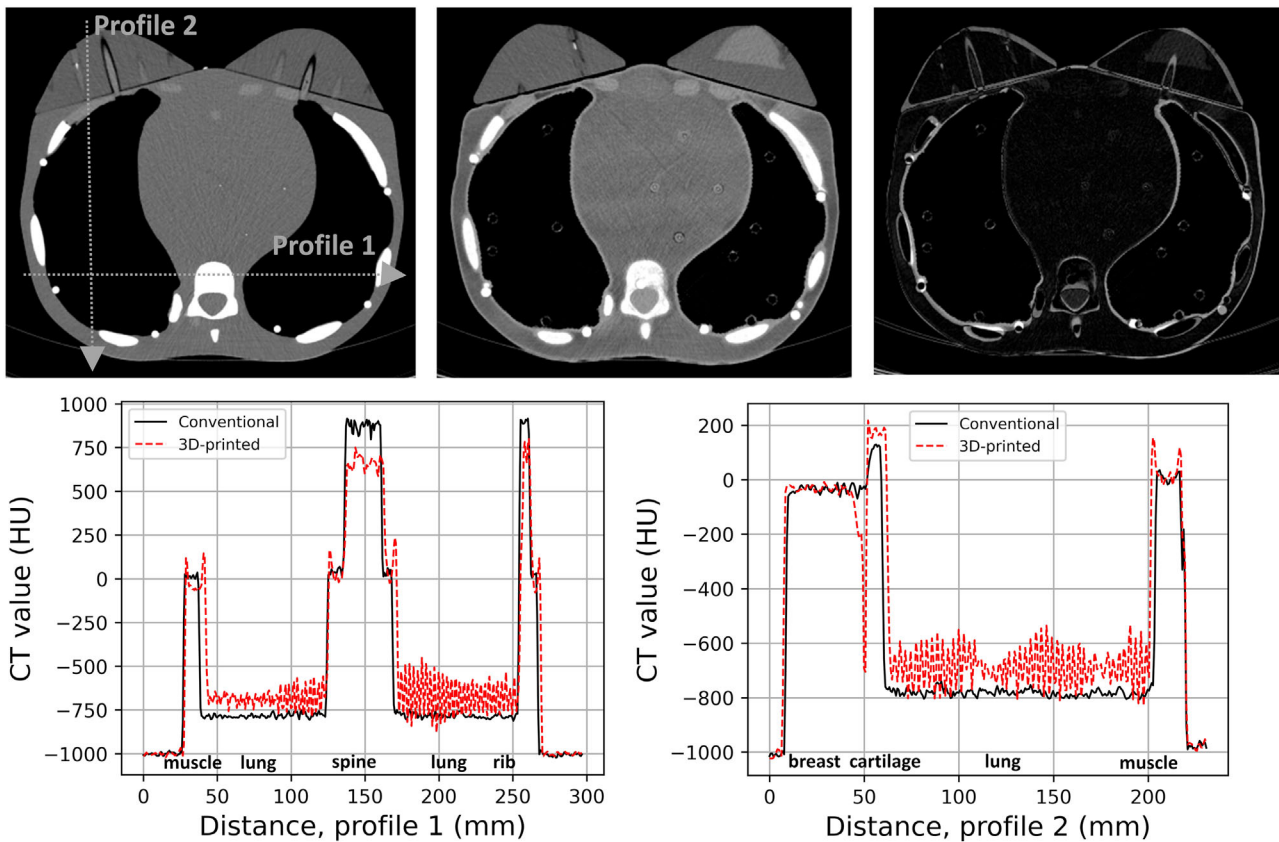
FIGURE 6 Upper row: CT images of the conventionally produced (left) and printed (middle) phantom slices as well as the difference image (right) (width: 1100 HU, center: 100 HU). Lower row: CT value profiles determined from the images of both phantom slices along the two directions indicated in the left CT image.

add-ons, respectively. This could be attributed to the shrinking of the ABS material during printing. Slightly undulating structures on the surface of the printed breasts are also present in the digital data; thus, they are not ascribable to the printing process.

CT images of the conventionally fabricated and 3D-printed phantom slices as well as a depiction of the difference of both images are shown in Figure 6. Both phantom slices match geometrically very well. This applies to the outer and inner shape as well as to the location of inner structures. Minor differences are visible at the lung boundaries, which are produced in the 3D-printed phantom with an infill density of 100% to stabilize the inner lung structure printed with an infill density of 30%. However, these differences are less than 1 mm and thus negligible. The volume of the printed breast add-ons appears to be smaller than that of the conventionally produced ones, which confirms the geometrical deviations. Some differences in the breast structure are explainable by additional bore holes and a plastic screw that were in the conventionally produced but not in the 3D-printed add-ons. The simplified glandular structure in one of the printed breast add-ons is clearly distinguishable from the adipose tissue, and it is char-acterized by a smooth transition between the different materials.

CT value profiles along a vertical and horizontal line through the conventional and printed phantom slices are shown in the lower row of Figure 6. The horizontal profile 1 passes through the muscle tissue, lung tissue, spine, and a rib; the vertical profile 2 passes through the breast, costal cartilage, lung, and muscle tissue. In general, both profiles confirm the good consistency of the inner geometries. For the printed lung, a charac-teristically structure in form of jags with a high spatial frequency is recognizable in both profiles, represent-ing the lines of the printed infill pattern (Figure 1). The second profile shows an airgap (red peak downwards) between the printed breast add-on and the printed phan-tom slice. Owing to the uneven surface of the printed phantom, the printed breast could not be placed as evenly in the phantom's torso as on the conventional phantom.

The mean CT values determined for the different types of tissue for both the conventional and the 3D-printed phantom are summarized in Table 3. Additionally, typical ranges of CT values for the relevant tissues as measured in real humans are given. Although the CT

TABLE 3 CT values (mean $\pm$ standard deviation in HU) for the considered tissues in the conventionally produced and 3D-printed phantom slices as well as typical ranges observed in humans.

Tissue	Conventional phantom	3D-printed phantom	Humans
Bones	860 $\pm$ 40	700 $\pm$ 50	300 to 1200[20]
Cartilage	110 $\pm$ 15	170 $\pm$ 20	120 to 260[21]
Muscle tissue	20 $\pm$ 20	30 $\pm$ 25	20 to 40[22]
Lung tissue	−780 $\pm$ 10	−690 $\pm$ 80	−500 to −900[20]
Adipose tissue (breast)	−40 $\pm$ 10	−30 $\pm$ 10	−95 to −50[20]
Glandular tissue (breast)	−	95 $\pm$ 15	−37 to 45[23]
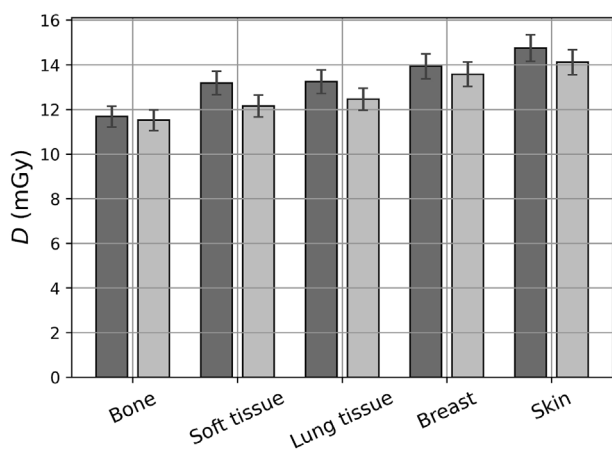
FIGURE 7 Absorbed doses, D, for a single scan measured with TLDs inside different tissues and at the skin, respectively the surface, of the conventionally produced (dark bars) and the printed (light bars) phantom slices of the chest. Error bars indicate the uncertainties of TLD measurements estimated at 4%.

values for the muscle and adipose breast tissue are similar in both phantoms, minor differences are visible for cartilage, where CT values are 60 HU higher in the printed phantom. Larger differences exist for the bones and lungs. For bones, the CT values are 160 HU lower in the printed phantom slice, this reflects the fact that no proper bone substitute material for 3D-printing has yet been identified. For the lungs, the mean CT values are 110 HU and the standard deviation 70 HU larger in the printed phantom slice. The higher standard deviation is owing to the printing pattern with reduced infill density (cf. Figure 1). Overall, the determined CT values measured are consistent with the ranges of CT values observed in humans, with exclusion of glandular tissue, which was slightly larger (50 HU) in the printed breast add-on.

Absorbed doses inside different tissues and at the skin of the conventionally produced and the printed phantom slices are presented in Figure 7. The dose to the homogeneously printed breast add-on (13.3 $\pm$ 0.5 mGy) was not considerably different from the dose to the add-on containing a simplified glandular structure printed with PMMA (13.8 $\pm$ 0.6 mGy). Therefore, only the mean dose of both breast add-ons

is shown in Figure 7, where it is compared to the dose to the conventionally produced ones. Considering the uncertainties owing to the TLD measurements, the dose to both phantoms is equivalent for all considered types of tissue.

4 | DISCUSSION

There is a need for fast and cheap production of individualized body phantoms suitable to determine image contrasts and absorbed doses for special examination scenarios in x-ray imaging, such as CT examinations of obese and pregnant patients who are not adequately approximated by conventionally produced anthropomorphic phantoms of reference persons. The production of phantoms using 3D-printing methods is a promising approach for this issue. To confirm this on a quantitative basis, we evaluated whether 3D-printed body phantoms are equivalent to their conventionally manufactured counterparts not only with respect to the transmission, but also the absorption of x-rays at the example of a typical CT examination of the chest region of a female.

The evaluation of a test series of printed material samples reveals that print settings (i.e., the print speed, infill density, height of layers, and location on the build plate) can systematically affect the relevant physical properties of the printed objects. This confirms previous findings concerning the infill density and pattern and provides additional insights on the effects of other relevant print settings. Because they depend on the type of printer used, it is strongly recommended to evaluate and minimize their effects at least before starting the production of phantoms. For example, the printer used in this study is characterized by a comparably large print bed, which complicates the exact calibration over the entire print region and explains the larger deviations between samples printed at different locations. Besides printing settings, the orientation of printed samples in the CT scanner is also relevant for the quantification of CT values in case of infill patterns that are not isotropic as already shown for the used line pattern in our previous paper.[10] For the phantom slice printed in the present study, the orientation was the

same as in the cubic samples, which makes the results transferable.

ABS was used to approximate the breast tissue, which was found to be a good equivalent for adipose tissue.[10] However, this material shrinks during cooling after the print.[24] A general solution for this problem would be to increase the volume of the 3D-object in the slicing software by a specific shrinking factor. This factor needs to be individually determined in a test print by comparing the deviation of the dimensions of the printed sample from its 3D-model. Although this behavior poses no problem when printing a simplified glandular structure with PMMA inside the ABS structure, the effect on the printing of realistic glandular structures or subcutaneous fat structures should be studied. Alternatively, there are other print materials similar to adipose tissue that might be less affected by this problem (i.e., nylon or high-impact polystyrene).[10] However, the material characteristics and printing behaviors should be considered to ensure a good adhesion between different thermoplastic materials in the MEX process. For the purpose of this study, the shrinking of ABS in printed subcutaneous fat structures was not investigated further, as the conventionally produced phantom that served as a template for the 3D-printed phantom parts does not differentiate between muscle and adipose tissue.

Although the CT values for muscle and adipose breast tissue were almost identical in the printed and the conventionally produced phantom, larger deviations were observed for lung tissue and bones (cf. Table 3). However, it should be considered that CT values of lungs and bones considerably differ intra- and inter-individually, depending on, for example, the age and sex.[25]

The CT value of printed lung tissue can be easily adjusted by changing the infill density. In contrast, the markedly lower CT values of printed bones result primarily from the different atomic composition of the used thermoplastic material printed with an infill density of 100%, which cannot be increased by the printing settings themselves but only by the addition of a material containing elements with higher atomic numbers during the printing step.[26]

However, neither the conventional nor the 3D-printed phantom separates between cortical bone, cancellous bone, and bone marrow, even if there may be differences of up to 1000 HU in the CT values between these substructures. Both phantoms contain in their skeleton a mean bone composition, which is a sufficient approximation for most purposes. Separate printing of each substructure is hampered by the lack of appropriate thermoplastic filaments and the number of materials that can be processed in a single print session.

Because mass densities have per definition no direct impact on the absorbed dose, the dose to the printed tissue-equivalent anatomical structures of the conventionally produced and 3D-printed phantom parts is consistent.

The limitations of this study are as follows:

First, a conventionally produced phantom of a female was reproduced through 3D-printing. However, conventionally produced phantoms cannot be regarded as absolute benchmarks, as they only approximate the human body in terms of its absorption and attenuation of x-rays. To overcome this limitation, image datasets of real persons should be used in further studies as templates for both 3D-printing and Monte-Carlo simulations, which would allow a realistic evaluation of printed body phantoms. This is part of an ongoing study.

In this context, it has to be referred to various concepts to print more realistic phantoms with the MEX technology published most recently. For example, by mixing two different filament materials with well-defined fractions during the printing step, realistic glandular structures or bone compositions can be produced.[26–28] In addition, more realistic lungs can be printed by selective adjustment of infill densities for individual lung regions.[29,30] Especially when it comes to patient-specific phantoms, these or similar concepts should be considered to obtain more realistic image contrasts.

Second, although the printer used in this study can process three materials in a single print session, it is not sufficient to print complex fine structures simultaneously using additional materials, such as realistic bone structures. To overcome this problem, the infill density can be adapted to imitate different tissues using the same thermoplastic material,[5,29] or different body regions can be produced separately as has been done in the present study in case of the breast add-ons. Alternatively, MEX printers with more print heads are available; however, they are more cost intensive.

5 | CONCLUSION

As demonstrated by a representative example, printed body phantoms can reproduce conventionally fabricated anthropomorphic phantoms with respect to attenuation and absorption of x-rays. An indispensable prerequisite is, however, that the print settings are carefully optimized. The reliability of cost-effective in-house 3D-printing of patient- or task-specific phantoms needs to be further evaluated in more detail compared to results obtained by Monte Carlo simulations.

CONFLICT OF INTEREST STATEMENT
The authors declare no conflicts of interest.

DATA AVAILABILITY STATEMENT

The data that support the findings of this study are available on request from the corresponding author.

REFERENCES

1. Mille MM, Griffin KT, Maass-Moreno R, Lee C. Fabrication of a pediatric torso phantom with multiple tissues represented using a dual nozzle thermoplastic 3D printer. *J App Clin Med Phys*. 2020;21(11):226-236. doi:10.1002/acm2.13064
2. Tino RB, Yeo AU, Brandt M, Leary M, Kron T. A customizable anthropomorphic phantom for dosimetric verification of 3D-printed lung, tissue, and bone density materials. *Med Phys*. 2021;49(1):52-69. doi:10.1002/mp.15364
3. Ehler ED, Barney BM, Higgins PD, Dusenbery KE. Patient specific 3D printed phantom for IMRT quality assurance. *Phys Med Biol*. 2014;59:5763. doi:10.1088/0031-9155/59/19/5763
4. Craft DF, Howell RM. Preparation and fabrication of a full-scale, sagittal-sliced, 3D-printed, patient-specific radiotherapy phantom. *J App Clin Med Phys*. 2017;18(5):285-292. doi:10.1002/acm2.12162
5. Hatamikia S, Kronreif G, Unger A, et al. 3D printed patient-specific thorax phantom with realistic heterogenous bone radiopacity using filament printer technology. *Zeitschrift fur medizinische Physik*. 2022;32(4):438-452. doi:10.1016/j.zemedi.2022.02.001
6. Choi Y, Lee IJ, Park K, et al. Patient-specific quality assurance using a 3D-Printed chest phantom for intraoperative radiotherapy in breast cancer. Original Research. *Front Oncol*. 2021;11. doi:10.3389/fonc.2021.629927
7. Madamesila J, McGeachy P, Villarreal Barajas JE, Khan R. Characterizing 3D printing in the fabrication of variable density phantoms for quality assurance of radiotherapy. *Physica Medica*. 2016;32(1):242-247. doi:10.1016/j.ejmp.2015.09.013
8. Savi M, Andrade MAB, Potiens MPA. Commercial filament testing for use in 3D printed phantoms. *Radiat Phys Chem*. 2020;174:108906. doi:10.1016/j.radphyschem.2020.108906
9. Okkalidis N, Chatzigeorgiou C, Okkalides D. Assessment of 11 available materials with custom three-dimensional-printing patterns for the simulation of muscle, fat, and lung Hounsfield units in patient-specific phantoms. *J Eng Sci Med Diagn Ther*. 2017;1(1). doi:10.1115/1.4038228
10. Kunert P, Trinkl S, Giussani A, Reichert D, Brix G. Tissue equivalence of 3D printing materials with respect to attenuation and absorption of X-rays used for diagnostic and interventional imaging. *Med Phys*. 2022;49(12):7766-7778. doi:10.1002/mp.15987
11. Leng S, Chen B, Vrieze T, et al. Construction of realistic phantoms from patient images and a commercial three-dimensional printer. *J Med Imaging (Bellingham, Wash)*. 2016;3(3):033501. doi:10.1117/1.JMI.3.3.033501
12. Tillery H, Moore M, Gallagher KJ, et al. Personalized 3D-printed anthropomorphic whole-body phantom irradiated by protons, photons, and neutrons. Article. *Biomed Phys Eng Express*. 2022;8(2)027004. doi:10.1088/2057-1976/ac4d04
13. Hazelaar C, van Eijnatten M, Dahele M, et al. Using 3D printing techniques to create an anthropomorphic thorax phantom for medical imaging purposes. *Med Phys*. 2018;45(1):92-100. doi:10.1002/mp.12644
14. Craft D, Burgett E, Howell R. EP-1435: evaluation of single material and multimaterial patient-specific, 3D-printed radiotherapy phantoms. *Radiother Oncol*. 2017;123:S765-S766. doi:10.1016/S0167-8140(17)31870-4
15. Kamomae T, Shimizu H, Nakaya T, et al. Three-dimensional printer-generated patient-specific phantom for artificial in vivo dosimetry in radiotherapy quality assurance. *Physica Medica*. 2017;44:205-211. doi:10.1016/j.ejmp.2017.10.005
16. Kim SY, Park JW, Park J, Yea JW, Oh SA. Fabrication of 3D printed head phantom using plaster mixed with polylactic acid powder for patient-specific QA in intensity-modulated radiotherapy. *Sci Rep*. 2022;12(1):1-10. doi:10.1038/s41598-022-22520-6
17. Schneider CA, Rasband WS, Eliceiri KW. NIH Image to ImageJ: 25 years of image analysis. *Nat Methods*. 2012;9(7):671-675. doi:10.1038/nmeth.2089
18. Fedorov A, Beichel R, Kalpathy-Cramer J, et al. 3D Slicer as an image computing platform for the Quantitative Imaging Network. *Magn Reson Imaging*. 2012;30(9):1323-1341. doi:10.1016/j.mri.2012.05.001
19. Brix G, Lechel U, Veit R, et al. Assessment of a theoretical formalism for dose estimation in CT: an anthropomorphic phantom study. *Eur Radiol*. 2004;14(7):1275-1284. doi:10.1007/s00330-004-2267-7
20. Kalra A. Developing FE human models from medical images. *Basic Finite Element Method as Applied to Injury Biomechanics*. Elsevier; 2018:389-415.
21. Ikeda T. Estimating age at death based on costal cartilage calcification. *Tohoku J Exp Med*. 2017;243(4):237-246.
22. Lev M, Gonzalez R. CT angiography and CT perfusion imaging. *Brain Mapping: The Methods*. Elsevier; 2002:427-484.
23. Schneider W, Bortfeld T, Schlegel W. Correlation between CT numbers and tissue parameters needed for Monte Carlo simulations of clinical dose distributions. *Phys Med Biol*. 2000;45(2):459.
24. Ramian J, Ramian J, Dziob D. Thermal deformations of thermoplast during 3D printing: warping in the case of ABS. *Materials*. 2021;14(22):7070. doi:10.3390/ma14227070
25. Batawil N, Sabiq S. Hounsfield unit for the diagnosis of bone mineral density disease: a proof of concept study. *Radiography*. 2016;22(2):e93-e98.
26. Tino R, Yeo A, Brandt M, Leary M, Kron T. The interlace deposition method of bone equivalent material extrusion 3D printing for imaging in radiotherapy. *Mater Des*. 2021;199:109439. doi:10.1016/j.matdes.2020.109439
27. Okkalidis N, Bliznakova K. A voxel-by-voxel method for mixing two filaments during a 3D printing process for soft-tissue replication in an anthropomorphic breast phantom. *Phys Med Biol*. 2022;67(24):245019. doi:10.1088/1361-6560/aca640
28. Okkalidis N, Bliznakova K, Kolev N. A filament 3D printing approach for CT-compatible bone tissues replication. *Physica Medica*. 2022;102:96-102. doi:10.1016/j.ejmp.2022.09.009
29. Okkalidis N. A novel 3D printing method for accurate anatomy replication in patient-specific phantoms. *Med Phys*. 2018;45(10):4600-4606. doi:10.1002/mp.13154
30. Mei K, Geagan M, Roshkovan L, et al. Three-dimensional printing of patient-specific lung phantoms for CT imaging: emulating lung tissue with accurate attenuation profiles and textures. *Med Phys*. 2022;49(2):825-835. doi:10.1002/mp.15407